Design and experiment of a sun-powered smart building envelope with automatic control

Qiliang Lin [a], Yanchu Zhang [a], Arnaud Van Mieghem [b], Yi-Chung Chen [c], Nanfang Yu [d], Yuan Yang [d], Huiming Yin [a,*]

[a] Department of Civil Engineering and Engineering Mechanics, Columbia University, United States
[b] Department of Electrical Engineering ESAT, Katholieke Universiteit Leuven, Belgium
[c] Department of Electrical and Computer Engineering, Tennessee State University, United States
[d] Department of Applied Physics and Applied Mathematics, Columbia University, United States

ARTICLE INFO

ABSTRACT

A novel sun-powered smart window blind (SPSWB) system has been designed and developed for the smart control of building envelopes to achieve the optimal internal comfort with minimum energy expenditure. Its self-powered sensing, controlling, and actuation significantly simplify the installation and maintenance of the system. The energy is harvested by the attached thin-film photovoltaic cells, after which it is voltage-regulated for the permanent storage into a rechargeable battery with 55% energy efficiency. The excessive heat absorbed by the solar cells is dissipated by a PVdF-HFP porous coating with more than 9% temperature reduction. The smart control of the energy harvesting and the cooling is achieved based on the blinds' surface temperature by an Arduino-based sensing, controlling, and actuating system, whose energy consumption is closely monitored. The energy equilibrium analysis is proposed for the self-powered design in any locations, and the optimal solar energy harvesting can be achieved by the proper adjustments of the window blinds angle with respect to the geographical location. The abundant energy that can be harvested validates the feasibility and the robustness of the system and proves its wide application potentials to the next generation of smart building envelope systems.

© 2020 Elsevier B.V. All rights reserved.

1. Introduction

The building sector is the largest consumer of energy. It was reported that 76% of electricity use and 40% of all U.S. primary energy use are consumed by the buildings sector [1]. Its share of electricity use has grown dramatically from 25% of U.S. annual electricity consumption in the 1950s to 40% in the early 1970s, and to more than 76% by 2012 [2]. In this sense, smart building management becomes significantly important to achieve the optimal interior comfort with minimal energy expenditure, by the continuous monitoring of the environment and the smart control of the major building appliances, such as heating, ventilation, and air conditioning (HVAC), lighting, and water heating etc. [3]. Research shows that a potential energy saving of 34.78% could be achieved by the smart buildings comparing to conventional buildings, through the optimal control of major building components like the heating, ventilation, air conditioning, and lighting systems [4].

The concept of smart building management has attracted significant attention in the civil engineering industry during the past decade. It provides the solution to achieve the optimal interior comfort with minimal energy consumption but would also require smart controlling algorithms and continuously monitored environmental data with Internet of Things (IoT) devices. Significant attention has been paid to the controlling algorithms thanks to the boom of artificial intelligence, with a lot of discussions about energy consumption forecast [5–7], smart grid technology [8], and in-room occupancy detection [9]. The importance of the sensor network is underestimated with fewer research and discussion. Considering the energy consumption of data acquisition, processing, and wireless communication, the bottleneck for sensing the environment is the limited time of operation due to the insufficient battery capacity [10]. For specific applications in the building environment, it could be very difficult to reach the sensing node to replace the battery, which can result in costly maintenance procedures on large scale. Therefore, the energy harvesting provides an excellent solution to elongate the battery lifetime and to reduce the cost and time in both installation and maintenance. Recently a thermoelectric-powered wireless sensing network platform

---

* Corresponding author.
  E-mail address: yin@civil.columbia.edu (H. Yin).

(TPWSN) was proposed as a self-powered platform for various sensors and prototyped completely inside the window frame with no compromise of the outlook [37]. It harvests energy from temperature difference across the window and feeds the sensors and the microcontroller for the continuous environmental monitoring and the wireless data transmission. However, the data acquisition is the first step of the smart building management and is followed by the data analysis in the controller and the responses via the actuators. The actuators consume much more power than the sensors and therefore require a stronger energy harvesting technology to achieve the self-powered stage.

The solar energy harvesting is by far one of the most developed and promising energy harvesting technology in recent decades and is therefore a suitable energy source for the actuators. After first invented in 1946, the modern solar cell industry has gone through three generations of development, with an efficiency up to 40% [11]. Among them, the silicon wafer solar cell, as the first-generation product, occupies most of the industry. The second-generation solar cell uses the thin-film technologies that significantly reduces the light absorbing layer from the 350 μm to the scale of 1 μm [12]. The newest generation of solar cell, although not commercialized yet, can reach the efficiency much higher than the previous generations [13]. During the past decade, wide range of photovoltaic applications have been observed in the building sector, especially the building envelope sector, thanks to the evolvement of building integrated photovoltaic and the considerable energy demand from building components.

Two major classifications are defined for the building photovoltaic systems: building integrated photovoltaic (BIPV) and building attached photovoltaic (BAPV) [14]. The BIPV is considered as a functional part of the building structure, or architecturally integrated into the building design. The most widely seen BIPV product is the BIPV roof, which is used to replace the original building roof, or to fit with a specific roof solution produced by the manufacturer [15]. The BIPV roof integrates the solar panels into the roof to provide both energy harvesting capability and the structural capability for the environmental loading. The concept of the building integrated photovoltaic thermal roof is later proposed to both harvest the additional thermal energy and cool down the PV for a better energy conversion rate [16–22]. The BIPV is also applied to the window/façade thanks to the development of transparent and semi-transparent solar cells, such that it can be integrated into the window/façade glass for both shading and energy harvesting purposes [23–26]. The transparency level varies from 16% to 41% for various models [15]. The BAPV is considered as an add-on to the building and is not directly related to the structure's functional aspect. The BAPV systems are usually standing or rack-mounted onto the superstructure such as building roof or curtain walls [27–29]. Although it is less studied in academia, the BAPV is widely applied to the industry thanks to its cost and retrofit advantages. The shading system, as an important attachment to the building window/façade systems, has significant exposure to the exterior environment and is therefore the perfect location for the BAPV systems. However, the research and application of photovoltaic to the shading system is limited. A recent PV-shading system called Lumiduct was proposed by attaching the concentrating photovoltaic module to the double-skin façade [30]. It optically concentrated solar light to a restricted area of solar cells to satisfy the needs of transparency and diffusivity. The Lumiduct has the potential for the self-powered media wall with integrated LED lights, but suffers from the limited area of PV cells for energy harvesting and the overly large system size for applications with restricted space. Another PV-integrated shading system was proposed by attaching the second-generation solar cells onto the window blinds, and the study was conducted from technical, economic, and political aspects for the potential application in Korea [31]. However, the

technical details were not discussed and the additional heat gain from the solar cells into the building was not addressed. The author focused on the energy generation from the window blind but overlooked the potential of the smart management system that could be powered by the harvested energy.

In this paper, a novel sun-powered smart window blinds (SPSWB) system is designed, prototyped, and tested to improve the energy efficiency of the building envelop by harvesting and storing the solar energy, improving the energy dissipation, sensing the surrounding environment, and automatically controlling the window blinds. The SPSWB is designed with flexible PV cells, coated with innovative porous coating for heat emittance, and automatically controlled by the motor and micro-controller based on the sensed data. Compared with the existing alternatives, the present SPSWB system is not only equipped with the energy harvesting component, but also with an innovative cooling system thanks to the porous PVdF-HFP coating, and a smart sensing and control system to actively monitor the environment for the optimal performance. This smart window blinds system extends the application of solar energy harvesting to the vast areas of building envelope components, self-powers various kinds of sensors and actuators, and function as an integrated platform to fulfill the building health monitoring and to test controlling algorithms for the next generation of the smart building management system. From the industrial perspective, it also provides a structured design guide and comprehensive test data that can be directly converted to market products. The self-powered functionality provides a clean and self-contained system and leads to tremendous cost saving by eliminating the hassles of the electrical wiring and battery maintenance.

The remainder of the paper is organized as follows. Section 2 presents the system architecture of the SPSWB system, which is decomposed into the PV-PVdF-HFP integrated window blinds, the power management, and the smart controlling subsections to elaborate the corresponding design philosophies further. Section 3 introduces the separated components and integrates them into a complete prototype. Its performance of energy harvesting and energy consumption is carefully tested and quantified. Section 4 discusses the energy equilibrium analysis of the SPSWB system based on the local weather measurements. Using the New York City (NYC) as an example, the balance between energy harvesting and consumption could be achieved for the eternal operation of the system based on the NYC's historical data. Section 5 summarizes the paper with some conclusive remarks.

2. System architecture and design philosophy

The sun-powered smart window blinds system is designed based on an aluminum window system with built-in window blinds, which is schematically shown in Fig. 1. The window blinds are covered with flexible photovoltaic cells on one side and coated with porous coating on the other side. The harvested energy from solar cells will self-power the operation and provide additional energy for external features. The heat absorbed by the PV cells will be dissipated through the thermally emissive coating made of porous poly vinylidene fluoride-co-hexafluoropropene (PVdF-HFP), which can drop the temperature of 5 ~ 8 °C lower than the ambient in summer, such that the overall energy efficiency could be increased. Sensors are integrated with continuous environmental monitoring and communicated to a local microcontroller for the preliminary data processing. The sensed data will serve as valuable information for the building management system for the optimization of the overall energy efficiency. Although only a temperature sensor is used in the current prototype, the system can be extended to various types of sensors for a comprehensive environ-
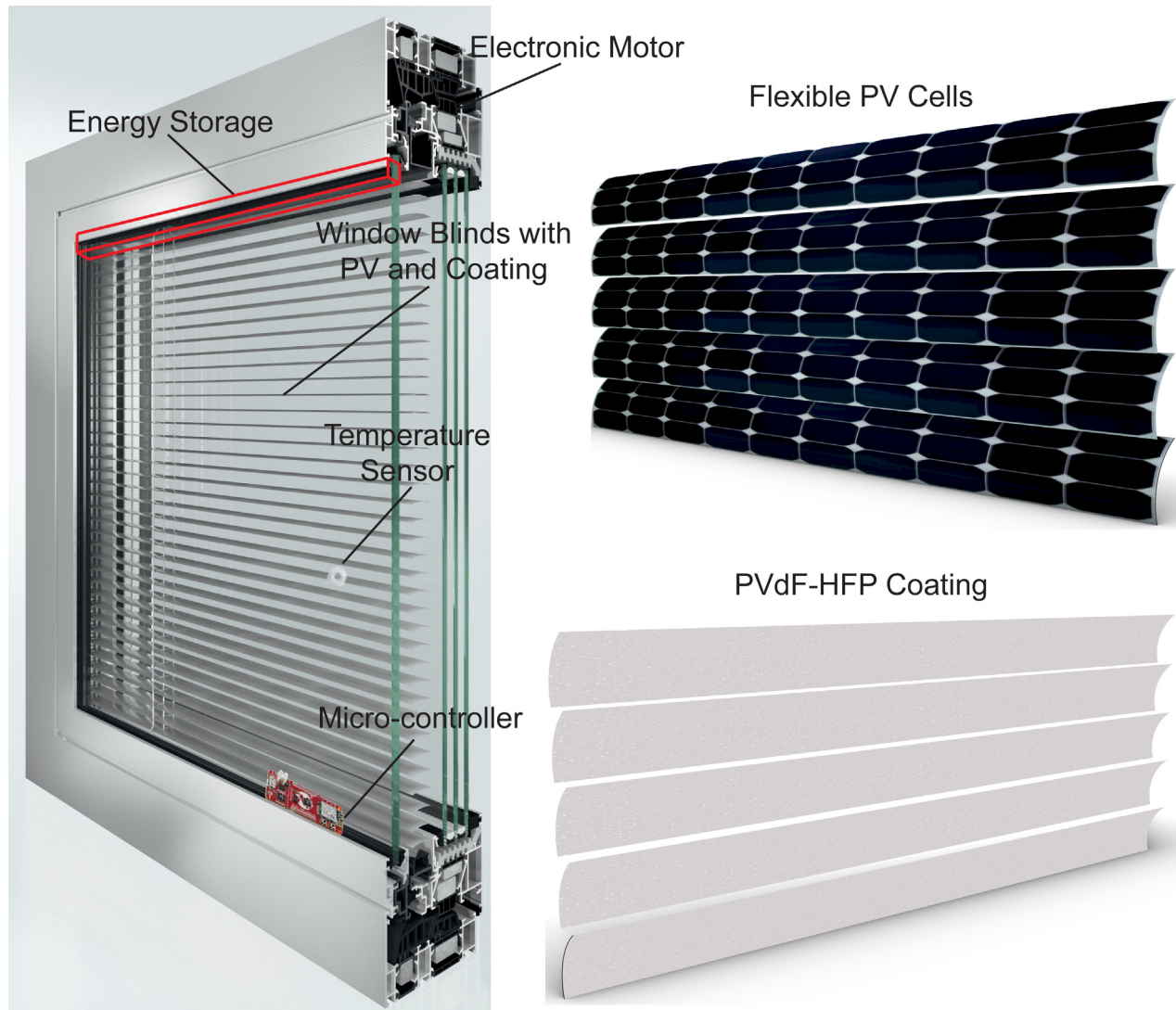
Fig. 1. Schematic drawing of the smart window unit and innovative blind blades.

mental monitoring, such as a light intensity sensor to detect direct sunlight, a moisture sensor for the raining leakage detection, a pollution sensor to monitor the quality of air, and an acoustic sensor for the noise level measurement. The corresponding responds of actuators, which is the motor in the scope of this research, are controlled via the microcontroller based on the sensed information, with the goal of achieving the optimal internal comfort with minimum energy expenditure.

The major components of the SPSWB and the relations are schematically shown in Fig. 2. The photovoltaic cells, the battery, and the power management system form the energy harvesting subsystem, while the sensors, microcontrollers and the motor compose the energy consumption subsystem. The self-powered design would require the harvested energy larger than the consumed energy within a certain timespan, and is discussed in detail in Section 4. The aluminum window system used in this study is the Schuco AWS120 window, where the physical dimensions are 0.9×1.5 m. The 24 V DCD22-2-E double shaft motor is integrated in the blind system and can provide the nominal torque of 0.6 N · m. It is worth to mention that the motor consumes the most power among all the components and shall be specially considered in the engineering. The nominal current consumption from the motor is 320 mA, which corresponds to the 7.7 W of nominal power consumption. The starting current of the motor is 1.45 A,

such that the instantaneous power consumption reaches 34.8 W. The battery system should be specially designed to satisfy the instantaneous power requirement of the motor. The detailed design and demonstration of each subsystem will be discussed in detail in the following subsections and the test performance will be discussed in Section 3.

2.1. Photovoltaic cells and solar reflective coating

The solar energy harvesting is achieved through the photovoltaic cells attached on the aluminum blinds. The thin-film photovoltaic cell, MP3-25 manufactured by PowerFilm, is selected and glued to the window blinds. The MP3-25 is a thin-film (0.22 mm) amorphous solar cell with great flexibility but compromised energy conversion efficiency, which is around 5% as advertised on its website [32]. The operating voltage of each PV cell is 3 V and the nominal power output is 90 mW. It is worth to mention that the surface of the MP3-25 is not UV stabilized and therefore would require special treatment for real applications. Each one of the window blinds is covered by 5 pieces of MP3-25 photovoltaic cells and connected in series to boost up the voltage output. The open-circuit voltage is around 14 V under in-room lighting, and around 19 V under the solar simulator. As is shown in Fig. 3, the area with the holes could not be fully covered by the PV cells in
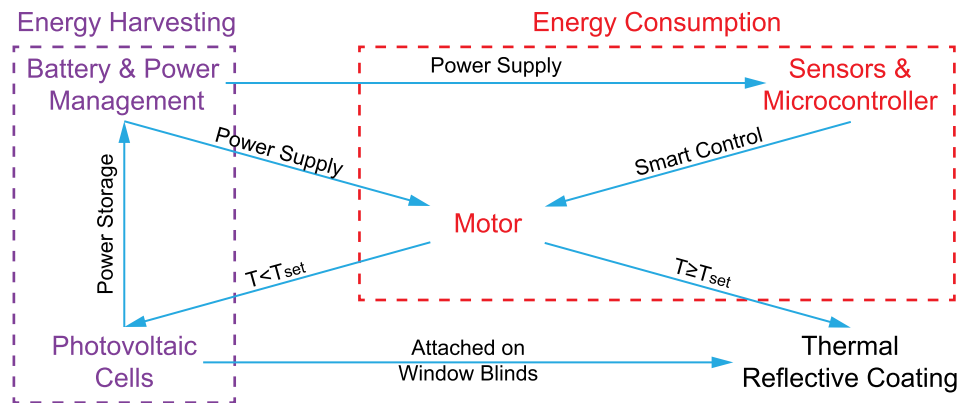
Fig. 2. Smart window blind system architecture.

the current prototype, and a higher voltage output could be expected if tailored cells could be manufactured. 18 pieces of blind slats were fabricated with PV cells and integrated into the window blind system as shown in Fig. 3. The PV covered blind slats are connected in parallel to boost up the current output for energy harvesting. Around 3 mA of short-circuit current is observed under in-room lighting and 400–850 mA under the solar irradiation of 850–1700 W/m². In the scope of this research, 18 pieces of blind slats are covered by PV cells, which corresponds to 30% of the total surface area of the window. More harvested power could be expected with a larger PV covered area.

The other side of the blind slats is covered with the porous PVdF-HFP coating, which has excellent passive daytime radiative cooling (PDRC) capability. The porous PVdF-HFP coating was recently invented to have a high hemispherical solar reflectance (0.96 ± 0.03), which minimized the solar heat gain, and a high long-wave infrared emittance (0.97 ± 0.02), that maximized the radiative heat loss. The coating was tested in Phoenix and achieved ~6 °C lower than the subambient temperature under 890 W/m² of solar irradiation, while the corresponding cooling performance of 96 W/m² was recorded under 750 W/m⁻² of averaged solar irradiation [33]. During the PVdF-HFP coating, a primer layer is first applied on the window blind surface to enhance the bonding strength, which takes approximately 10 min to dry. Then, the polymer coating is sprayed onto the blinds via a commercial spray gun Flexio 590 from Wagner Spraytech for six times at an interval of ten minutes. The polymer coating is initially liquid and turns into a white-colored porous solid film quickly after exposed to the air. Five window blinds are coated with the PVdF-HFP as is shown in
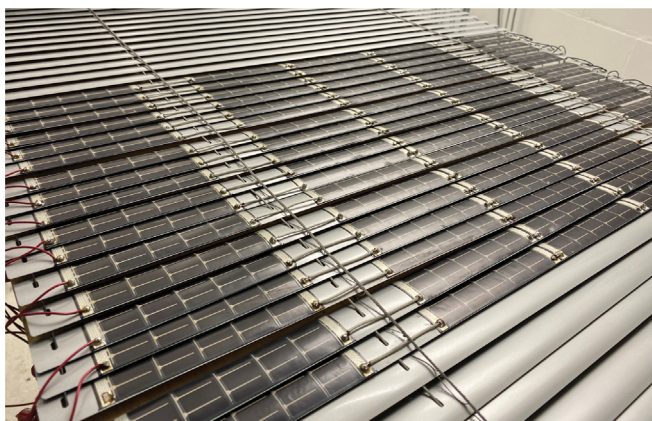
Fig. 4 and attached with PV cells on the other side to test the cooling performance.

2.2. Battery and power management system

The majority of the solar energy is generated when the sun is shining brightly, but virtually none is captured at night or in substantial cloud cover. Therefore, an energy storage unit must be introduced to account for the intermittency of the solar energy harvesting. As the major energy consumption component, the DCD22-2-E double shaft motor requires a 24 V power input with a start-up power requirement of 34.8 W. In order to meet the start-up current requirement, three 18650 lithium-ion batteries are connected to make a 12 V energy storage unit, as is shown in Fig. 5, and is managed by a battery management circuit for the over charge and over discharge protection. The LTC3780 buck boost converter is applied to stabilize and to regulate the voltage to 12 V for the battery charging. It automatically adjusts the internal resistance for the optimal power extraction from PV cells. The voltage is then taken up to 24 V with the help of a voltage booster for the power supply of the DCD22-2-E motor.

2.3. Sensors and microcontroller

The photovoltaic cells attached on the window blinds convert solar energy into electricity, but also absorb the solar thermal energy and increase the internal temperature. The out-facing solar
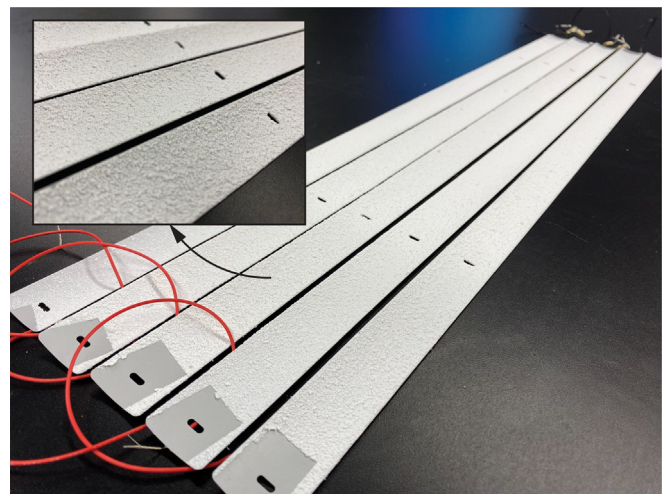

Fig. 3. PV integrated smart window blind.

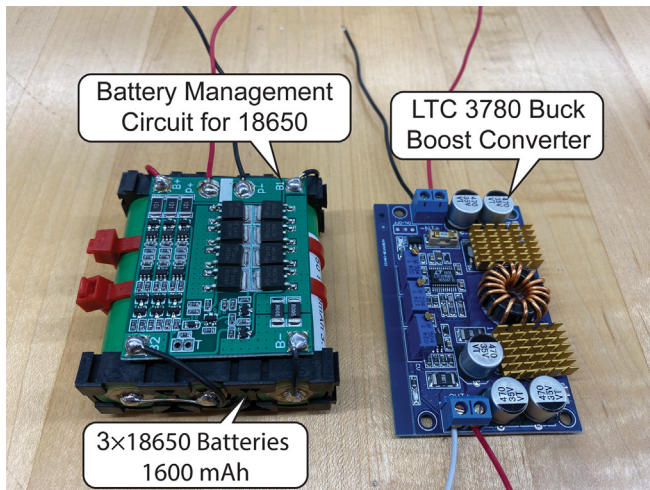Fig. 4. PVdF-HFP coating on the other side of the window blind.

Fig. 5. The 18650 battery pack and the LTC3780 buck boost converter.

cells on a hot summer day will significantly increase the temperature and compromise the internal comfort. Therefore, a smart controlling system is needed to monitor the surface temperature of the window blinds and to utilize the radiative cooling capability of the porous PVdF-HFP to dissipate the heat when the temperature is above a prescribed threshold. The Arduino Uno R3 development board is used as the microcontroller to collect the temperature measurements from the DS18B20 thermometer and to conduct logical decisions as when to rotate the window blinds. A dual H-bridge module, L298N, is used to switch the polarity of the applied voltage on the motor, such that the rotating direction of the motor can be digitally controlled by the signal from the microcontroller. The physical components of the Arduino Uno and the H-bridge are shown in Fig. 6 and the schematic drawing of the connections is shown in Fig. 7. The input signal is connected to the lower side of the H-bridge. Ranging from left to right one can find the 24 V power input from the battery, the ground, and 5 V logic power supply signal from the Arduino Uno. The advantage of having a 5 V signal is that the H-bridge can be turned off completely by the controller, meaning that no current will go through when the motor is not working. The output screw-terminals are located on the left and right of the H-bridge, both of which are connected to the motor with one wire serving as the positive and the other as ground wire. The output signal is equal to the 24 V power input and the polarity is controlled via the 5 V control signals. The deep
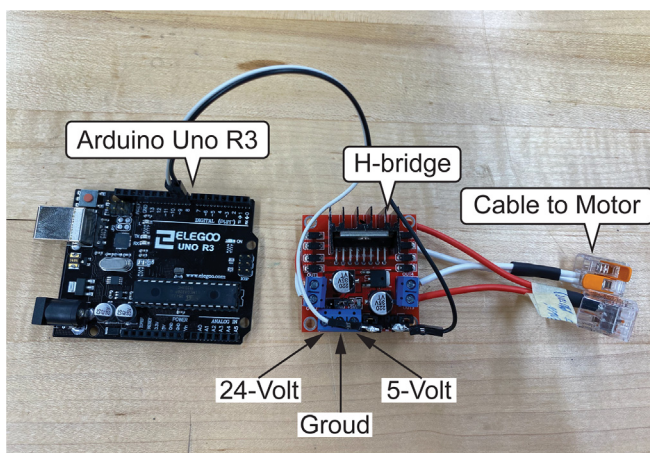
sleep mode is activated in the Arduino Uno and every 8 s, the system will wake up from the deep sleep to collect the temperature measurement from the thermometer. It can wake up after the Watchdog-timer finishes or by a manual interrupt signal, as by example of pushing a button. The microcontroller will then compare the temperature measurement with the predefined temperature thresholds and decide whether to send out the signals for the motor control, after which it will go back to deep sleep and wait for another cycle.

3. System integration and performance demonstration

Based on the system architecture and the key design philosophies in the previous section, the components of the SPSWB are integrated to formulate a complete prototype in this section and tested for the energy harvesting and the energy consumption performance, which are elaborated in Subsection 3.1 and Subsection 3.2 respectively.

3.1. Energy harvesting performance

The energy harvesting performance of the SPSWB is tested in the Carleton Laboratory at Columbia University. The window blinds are lying on a test table and exposed to the artificial solar irradiation generated by the 4000 W ATLAS MHG Solar Simulator, as is shown in Fig. 8. The distance between the solar simulator and the window blinds is 1.14 m. A pyranometer is placed close to the system and connected to the data acquisition system (DAQ) for the solar irradiation monitoring. Since the detector of the pyranometer is slightly higher than the PV cells, the measured solar irradiation is slightly larger than the received irradiation on PV cells. The current–voltage (IV) curves under different solar irradiation levels are measured by the Seaward PV210 solar tracer, in order to identify the maximum power output and the corresponding external resistance. Since the PV efficiency varies with the change of temperature, a thermocouple is also attached to the surface of the blind slats to monitor the temperature of PV cells via the DAQ continuously.

Both temperature and solar irradiation effects to the PV power outputs are investigated in the test. Since the exposure of the solar irradiation will increase the PV temperature and thus influence the power output, the temperature influence is addressed first by fixing the solar irradiation and test the IV curve under different temperature conditions. The I-V curves under 1263 W/m^2 solar irradiation and different temperature conditions are plotted in Fig. 9 (left). It is seen that the temperature influences more on the open-circuit voltage output but has a negligible impact to the short-circuit current output. The corresponding relationships between the power output to the external resistance are shown in Fig. 9 (right), from which it is observed that the power outputs lie between 6 W and 6.5 W, and that the 20 °C temperature difference will generate approximately 6% performance compromise. The optimal power output points and the corresponding external resistances are captured from Fig. 9 (right), and plotted versus the different temperature conditions in Fig. 10. The linear relationships to the temperature are observed for both the optimal power output and the external resistance.

After the temperature effects are addressed, the solar irradiation effects on the I-V curve and the optimal power output can also be addressed. Similar tests are carried out under different solar irradiation levels from 859 W/m^2 to 1709 W/m^2 after the temperature stabilized. The temperature influence can be offset by the relationships obtained from Fig. 10. The I-V curves are plotted in Fig. 11 (left), and it is observed that the solar irradiation has a significant influence on the short-circuit current, while almost no
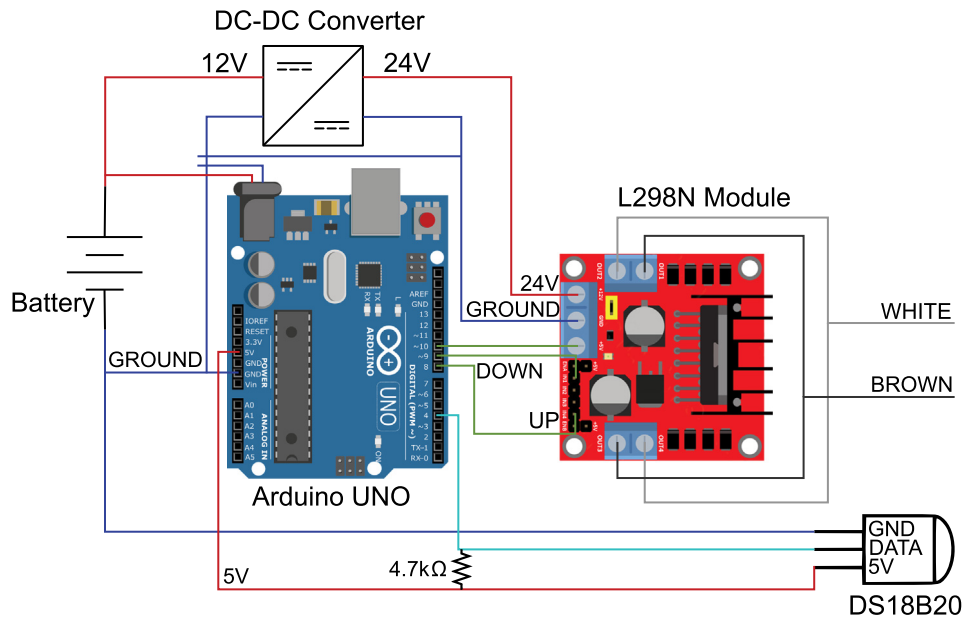

Fig. 6. The Arduino Uno R3 and the H-bridge.

Fig. 7. Schematic drawing of the connections in the controlling system.
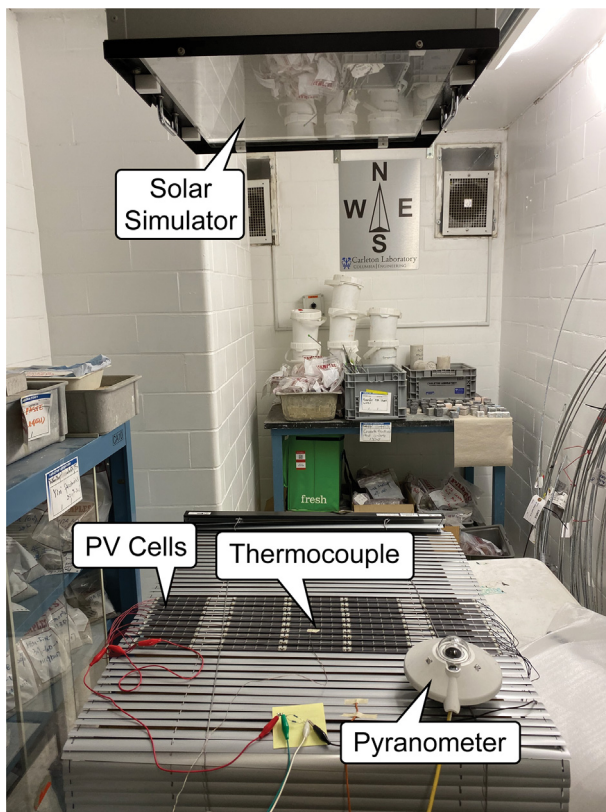
Fig. 8. Test configuration for the maximum power output of solar window blind.

influence on the open-circuit voltage. The corresponding power output to the external resistance is given in Fig. 11 (right), from which a clear linear trend is observed between the optimal power output and the solar irradiation. The relationships between power output and external resistance under different solar irradiations are plotted in Fig. 12. Therefore, the best power output and the corresponding resistance can be calculated for all cases, given the

solar irradiation and the temperature condition, with the help of bilinear interpolation and extrapolation of the current test results.

The optimal power output under every solar irradiation condition is extracted to compare with the input power from the solar simulator, such that the overall efficiency of the PV cells is calculated and listed in Table 1. It is seen that the overall efficiency lies around 2%, and gradually attenuates to 1.5% with the increase of the solar irradiation. The energy efficiency is lower than the claimed 5% and is due to the potential overlapping of the window blinds and the high temperature during the tests. In real applications, the overlapping cannot be avoided, but the solar irradiation will be much smaller, meaning that the temperature will be lower than the measurements. Therefore, it is projected that the efficiency in the real application will be around 2.5%.

The five PVdF-HFP coated blind slats are integrated into the window system and tested under the solar simulator so as to quantify the cooling performance of the coating. Similar testing configuration as described in Fig. 8 is set up. Two testing tables are bridged together with metal frames such that empty space for the heat dissipation can be generated. Both coated PV blinds and not-coated PV blinds are sitting on top of the metal frame and about 1.07 m below the solar simulator. Six different levels of solar irradiation ranging from 780 to 1700 W/m^2 are cast to increase the surface temperature of the blinds, which will gradually stabilize in 5 min. The temperature measurements are taken for both coated and un-coated PV blinds via the thermocouples attached at the center of the blinds, and are plotted in Fig. 13. Thanks to the PVdF-HFP coating, an apparent temperature reduction has been observed in the tests and the maximum drop can be as much as 7.6 °C under the solar irradiation of 1700 W/m^2, which corresponds to 9.31% of the temperature reduction and approximately 4% increase of PV power output. Less significant improvement is expected under weaker solar irradiation, and under the solar irradiation of 780 W/m^2, a 4 °C reduction of the surface temperature is observed. It is worth to mention that the tests were conducted in a confined room with limited air ventilation, and the room temperature reached 35 °C under 850 W/m^2 of irradiation, which compromised the passive cooling performance of the coating. A more substantial temperature reduction can hence be expected for the application in an open space.
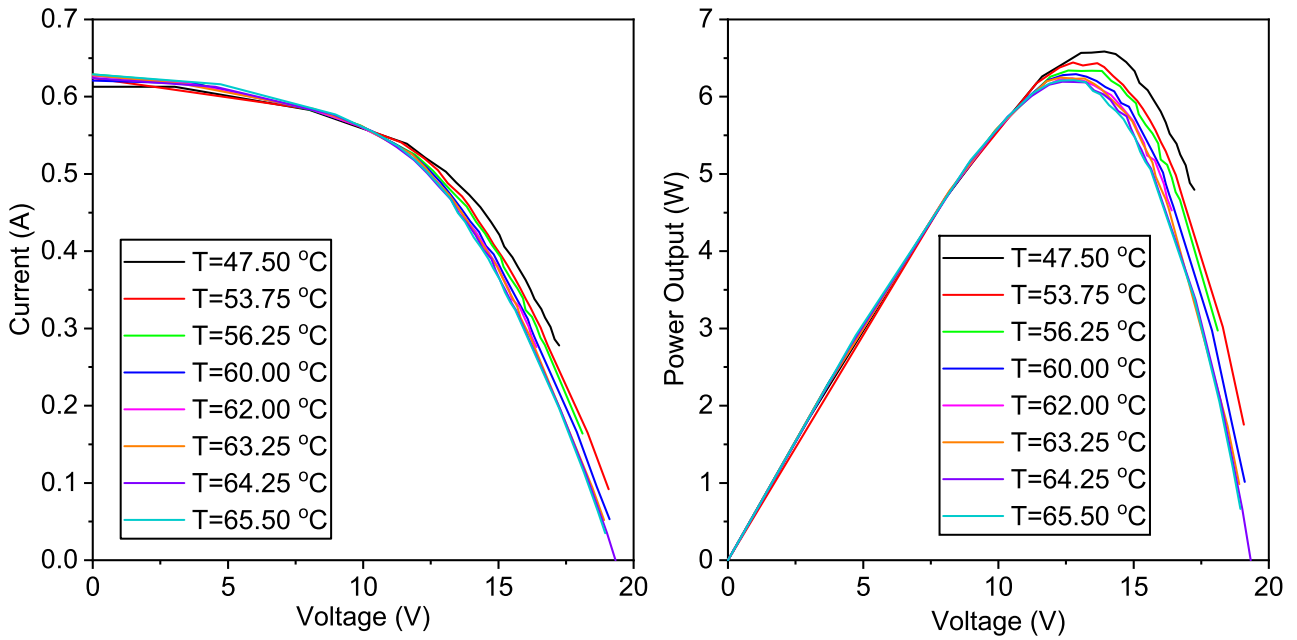
Fig. 9. Current and voltage relationships (left) and power output and external resistance relationships (right) under 1263 W/m² solar irradiation and different temperature conditions.
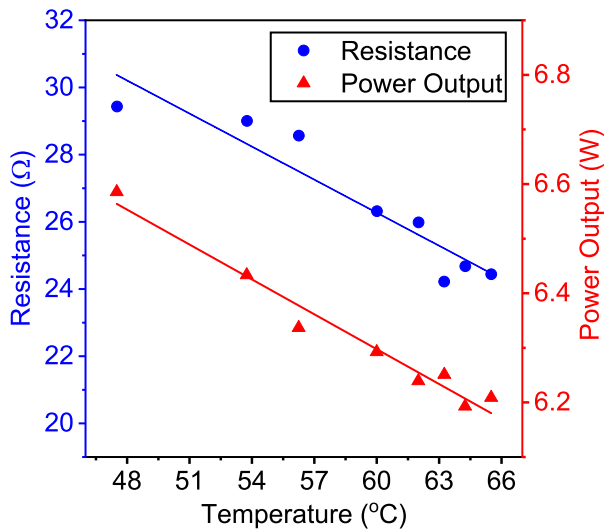

Fig. 10. Temperature influence on the optimal power output and external resistance under 1263 W/m^2 solar irradiation.

The harvested power from the photovoltaic cells is regulated to 12 V via the LTC3780 buck boost converter and charged to the battery through the battery management system. The charging process and the corresponding efficiency are continuously monitored by the data acquisition system as schematically described in Fig. 14. The tests are conducted under two solar irradiations of 760 W/m² and 1190 W/m², each of which lasts for approximately 20 min.

Each PV-integrated blind slat is connected with an N4007 diode to prevent the reverse current to neighboring blinds, each of which will take approximately 0.7 V. A resistor of 1.7 Ω is placed between the PV cells and the LTC3780 to monitor the direct current output with the help of the Data Acquisition (DAQ) system, at the frequency of 20 Hz. The current and power measurements directly from the PV cells are plotted in Fig. 15. With the help of the max-

imum power output in Fig. 11 (right), the total available power, the power into the converter, and the wasted power due to diodes and resistors are calculated and listed in Table 2, where an overall efficiency of 75% − 80% is achieved. Further improvement of the energy conversion efficiency could be achieved by a proper engineering and optimization of the buck-boost converter.

The average voltage measurements for both cases are 11.95 V and are stable throughout each test, which is seen by the similar patterns between the current and power distributions. While the voltage corresponding to the optimal power output is 13.43 V and 12.82 V for $I = 858.6$ W/m² and $I = 1166$ W/m², respectively, according to Fig. 11 (left). The voltage difference is due to the diode and the resistor between the converter and the PV cells. Therefore, the optimal power extraction of the LTC3780 is validated by the match of the voltage measurements. It is worth to mention that the smooth current measurement in Fig. 15 is obtained by taking 10 s of moving average of the original intermittent data.

After the energy from the PV cells is collected and voltage-regulated by the LTC3780, it is sent to the battery via the battery management system for the permanent storage. In order to quantify the efficiency of the battery management circuit, the current directly charged into the battery is measured and plotted together with the current into the LTC3780 in Fig. 16 for comparison. Due to the limited power the PV cells can provide, the energy density is not enough for stable current output, which makes current measurements intermittent with a small cyclic period. In order to have a better observation of the process, a detailed observation of the cycle is plotted in Fig. 17. It is seen that the current before and after the LTC3780 follows the same dynamic pattern. The battery charging current increases as the PV output current increases, and decreases as the PV current decreases. This behavior is due to the dynamic of LTC3780 internal resistance. The LTC3780 swipes its internal resistance to capture the maximum power input from the PV cells. It also tries to satisfy the user-defined current requirement at a stable level. When the minimum current requirement could not be met, the LTC3780 will continue to swipe its internal resistance and therefore causing the fluctuation of the current measurement. It is seen that the proportion of the high-current
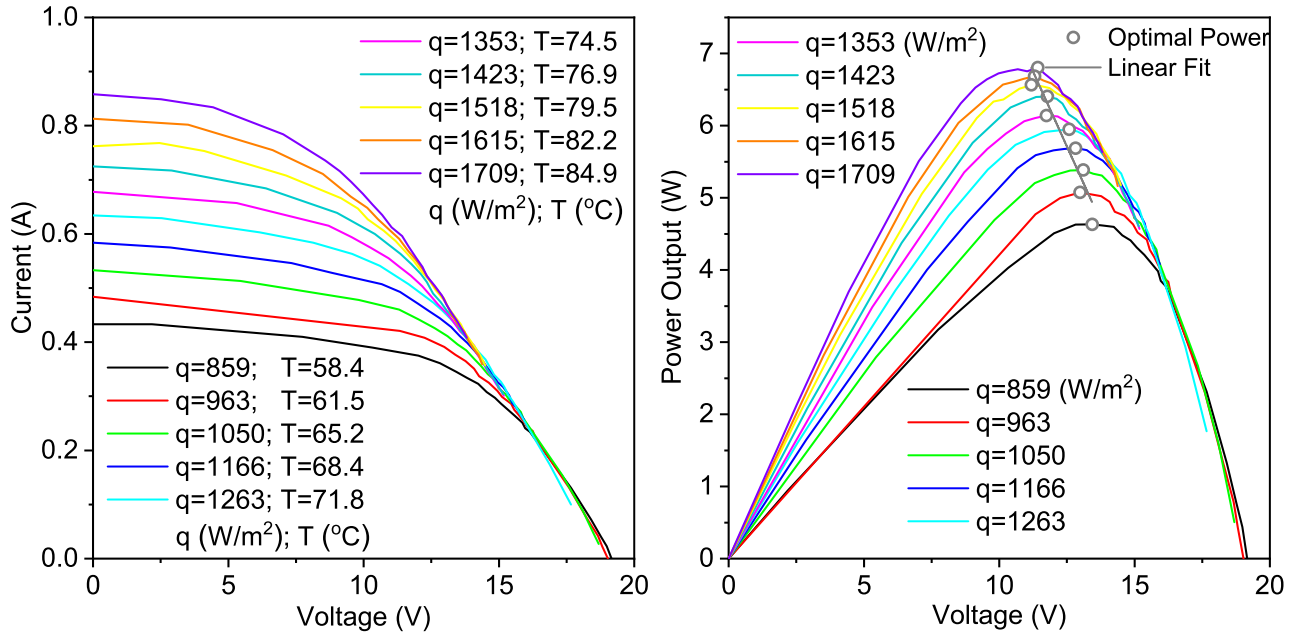
Fig. 11. Current and voltage relationships (left) and power output and external resistance (right) under different solar irradiation levels.
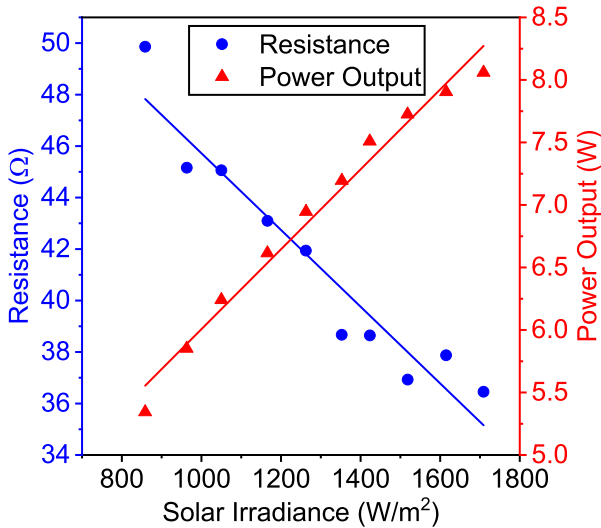

Fig. 12. Solar irradiation influence on the optimal power output and external resistance.

phase is largely increased in the 1190 W/m^2 case than in the 760 W/m^2 case while the peak values are very close to each other. Therefore, with larger input power, the LTC3780 will provide a greater proportion of the high-level current output and eventually provide the continuous current output. It is worth to mention that the harvested energy in the real application will be much smaller

than the lab test condition, due to the indirect sunlight and the weaker light intensity, therefore the fluctuation of current will be likely to occupy the majority of time in real applications. The energy conversion rate will be compromised and further optimization of the voltage regulating system shall be conducted and studied in the future.

The intermittent current measurements in Fig. 16 are transformed to a continuous distribution via a moving average over the surrounding 10 s and are plotted in Fig. 18. The averaged result is relatively stable across the testing period and the into-battery current of 0.27 A and 0.34 A is observed for the light intensity 760 W/m^2, and 1190 W/m^2, respectively. The detailed voltage and current measurements, as well as the power and efficiency analysis are listed in Table 3. It is seen that an overall efficiency of 70% is achieved for both cases from the PV output to the battery. Nearly 30% of the energy loss comes from the energy converter, the battery management system, the diode, and the resistor. It is worth to mention that the input voltage and the output voltage of the buck booster converter are very close in the test, and a slight difference of system efficiency is expected if the input voltage deviates from the output voltage.

The overall energy efficiency of the system reaches 58% and 52% under 760 W/m^2 and 1190 W/m^2 of solar irradiation intensity. Although the energy input of the second test is 1.56 times larger than the first test, as quantified by the rate of solar irradiation intensity, the overall current charged into the battery is only 1.26 times larger. The additional amount of energy is dissipated into the environment via the PV cells, the converter, the diode, and the resistor. In order to monitor the energy storage process, the

Table 1
The input and output power of PV cells and the corresponding efficiency.

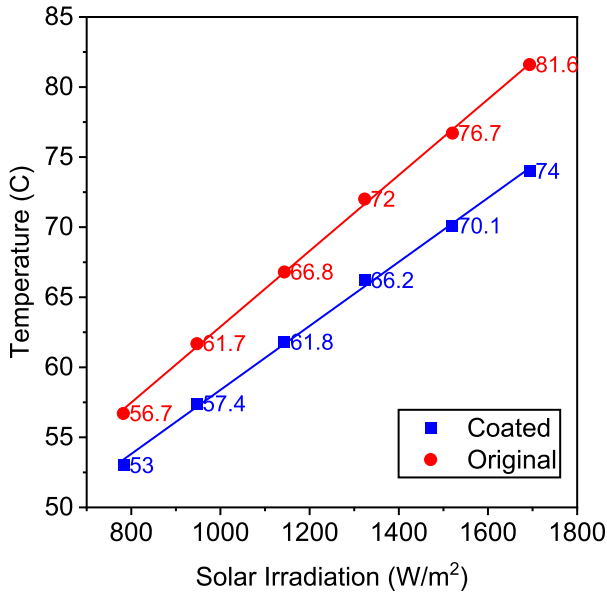| Solar irradiation (W/m^2)	859	963	1050	1166	1263	1353	1423	1518	1615	1709
Area (m^2)	0.26	0.26	0.26	0.26	0.26	0.26	0.26	0.26	0.26	0.26
Input power (W)	220	247	269	299	324	347	365	389	414	438
Temperature (°C)	58.4	61.5	65.2	68.4	71.8	72.6	75.0	77.6	80.3	83.0
Output power (W)	4.63	5.07	5.38	5.69	5.95	6.14	6.40	6.56	6.69	6.78
Efficiency (%)	2.10	2.05	2.00	1.90	1.84	1.77	1.75	1.69	1.61	1.55

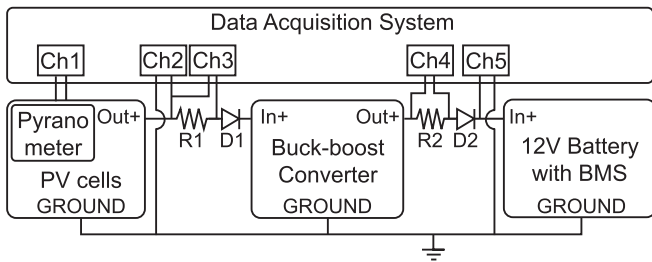**Fig. 13.** Coated and un-coated PV blinds temperature under different solar irradiation.

Fig. 14. Schematic drawing of energy management and storage system from PV to battery.
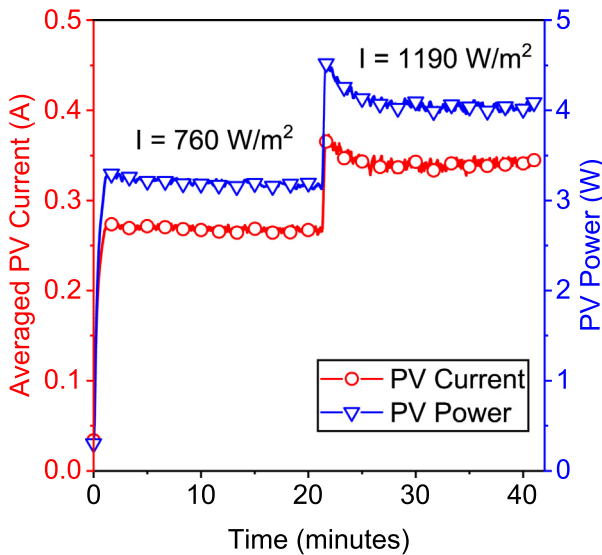

Fig. 15. Current and power output from the PV cells.

Table 2
Power availability and the energy efficiency from PV into LTC3780.

Solar intensity (W/m²)	760	1190
Total available power (W)	4.00	5.50
Power consumed by diode (W)	0.19	0.24
Power consumed by resistor (W)	0.12	0.20
Miscellaneous waste (W)	0.49	1.02
Power into converter (W)	3.20	4.04
Energy efficiency	80%	74%
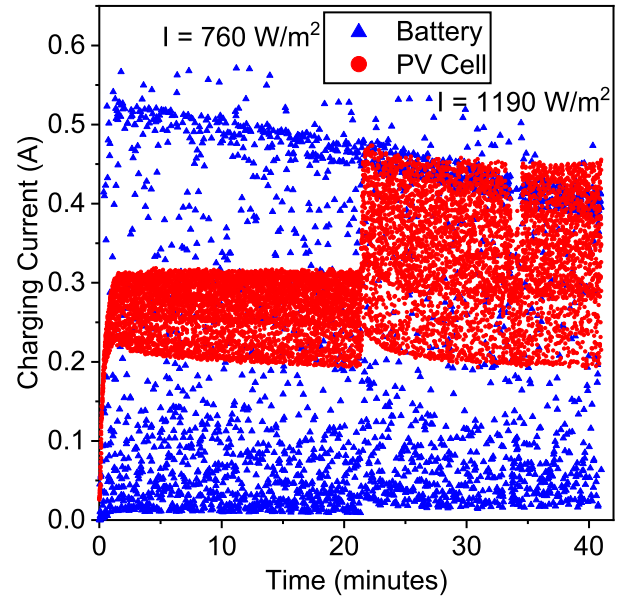
Fig. 16. PV output current and battery charging current.
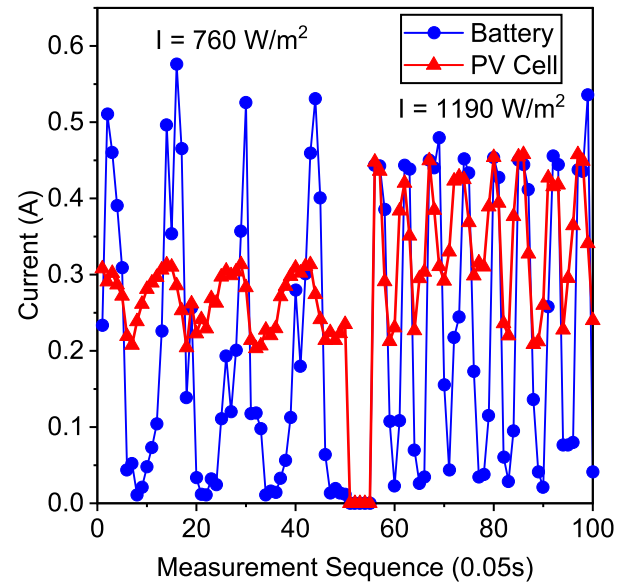
Fig. 17. Detailed cycles of PV output current and battery charging current.

1190 W/m² in the last 20 min. The battery voltage keeps increasing during the test and fluctuates at a period close to 1 min. Although no significant change of the battery voltage increase rate has been observed, the overall charging process goes smoothly at a rate of approximately 0.7 V/hour.

battery voltage is recorded and plotted in Fig. 19, where the test is conducted under the 760 W/m² in the first 20 min and under the

Fig. 18. Moving averaged result of PV output current and battery charging current.

Fig. 19. Battery voltage measurement over 40 mins.

Table 3
Power consumption and efficiency from LTC3780 into battery.

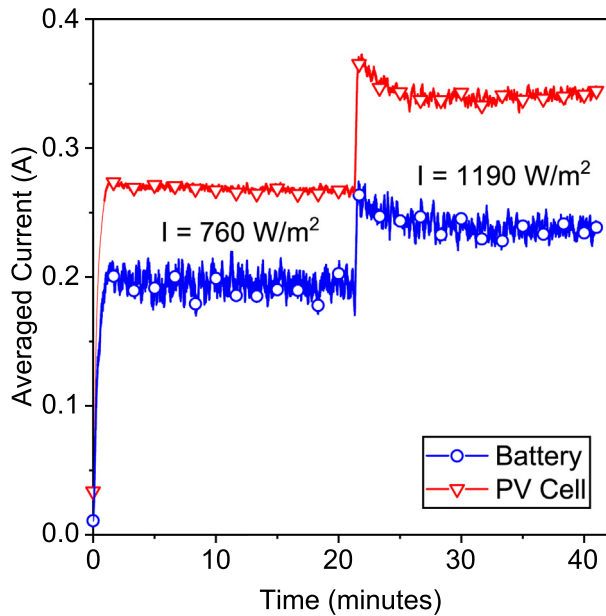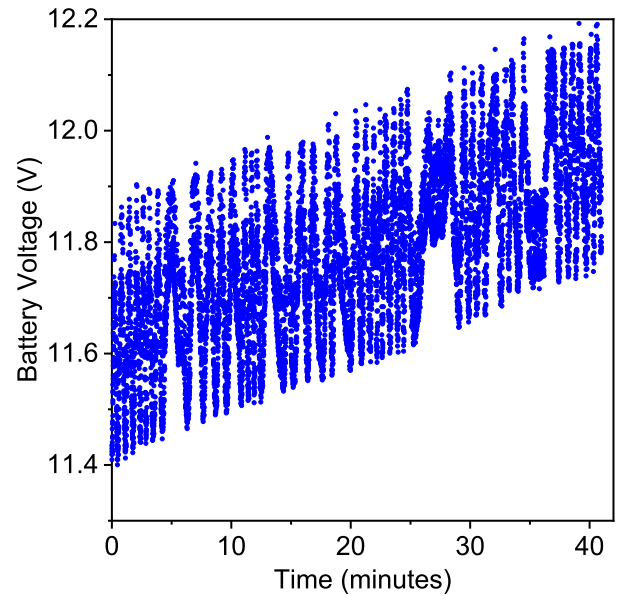|	Scenario	Light intensity = 760 W/m²	Light intensity = 1190 W/m²
Before LTC3780	Voltage (V)	11.90	11.90
	Current (A)	0.27	0.34
	Power (W)	3.20	4.04
After LTC3780	Battery voltage (V)	11.80	11.80
	Current into Battery (A)	0.19	0.24
	Power into battery (W)	2.30	2.83
	Diode consumed (W)	0.14	0.17
	Resistor consumed (W)	0.06	0.10
Efficiency		71.88%	69.98%

3.2. Energy consumption requirements

The self-powered design would require the harvested energy larger than the consumed energy from the sensors, microcontroller, and motor. The continuous power consumption monitoring is conducted via the data acquisition system in the test configuration described in Fig. 20. The window blinds are hung vertically from the ceiling and three-point fixed with nylon rope, such that the motor can be used to rotate, lift and lower the blinds. The ATLAS MHG Solar Simulator is used to artificially cast solar irradiation in order to test and calibrate the performance of the controlling system. The simulator is placed horizontally on a testing table for the horizontal irradiation and adjusted at the same distance from the blinds with the previous tests. The lowest solar irradiation output is chosen and the equivalent solar irradiation of 760 W/m² is received by the window blinds. A DS18B20 digital thermometer is used for temperature monitoring and attached to the PV surface as shown in Fig. 20. The use of a digital sensor over an analog sensor provides a greater accuracy and possibility to validate the reading. The sensed temperature data is compared with the prescribed temperature thresholds to determine the controlling responses. It is worth to mention the that window blinds cannot rotate 180° due to the mechanical connection to the motor. The
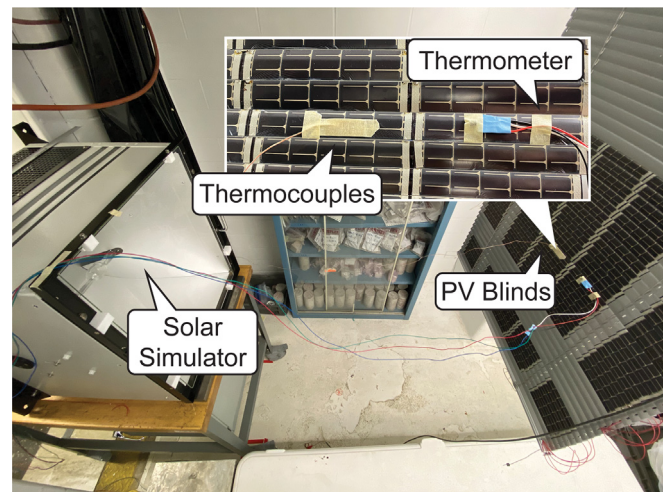

Fig. 20. Test configuration of the solar simulator and the window blinds.

schematic drawing of the blind is shown in Fig. 21 and a maximum rotation angle of 144° is mechanically prescribed. Moreover, a slight compromise of the cooling performance is expected since the non-PV side can only face the ground rather than the sky.

Two temperature thresholds $T_{high} = 47°C$ and $T_{low} = 42°C$ are predefined as thresholds for a hysteresis-loop in the microcontroller, such that the cooling process starts when the temperature measurement is higher than T_{high}, and the PV harvesting resumes when the temperature measurement is lower than T_{low}. The thermometer measurement is not readable for a standalone system with no wireless communication, and thus the thermocouple is attached to the same window blind as shown in Fig. 20, to serve as an indicator of the surface temperature. The measurements from the thermocouple and thermometer are recorded via the data acquisition system and the Arduino Uno, respectively, and plotted in Fig. 22 for comparison. Although the thermocouple measurement is slightly different from the thermometer, the dynamics of the temperature variation are successfully captured in both measurements. Therefore, the thermocouple is used as the indicator
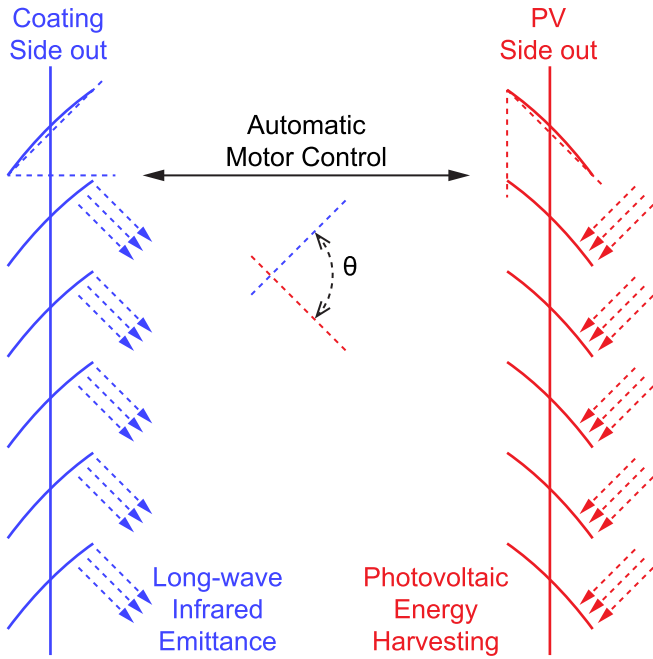
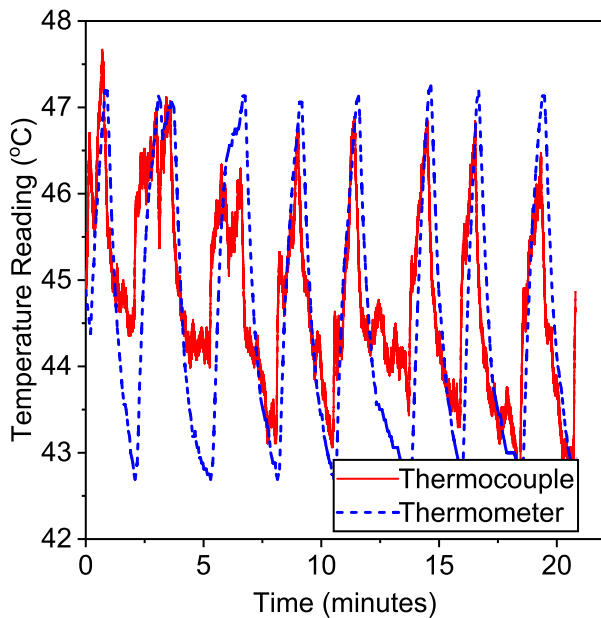Fig. 21. The rotating mechanism of the smart window blinds.

Fig. 22. Temperature measurement from thermocouple and thermometer.

of the surface temperature and the motor control when the thermometer measurement is not available.

Notice that the two temperature thresholds are chosen for the prototype demonstration and the energy consumption measurement. Further studies are needed to quantify the impact of the solar energy harvesting to the in-room temperature, such that the optimal temperature thresholds could be determined with the best system performance and the minimum compromise of the internal comfort.

The current output from the battery is monitored via the voltage measurement of a 1.43-ohm 25-watt resistor via the data acquisition system. Since the voltage from the battery is fixed at 12 V, the battery current output represents the total energy con-

sumption. In Fig. 23, the dynamic of the battery current output and the temperature variation are plotted in blue and red dots, respectively. If the surface temperature reaches the preset threshold temperature points, the H-bridge is open and the motor is activated for the rotation, which is observed as the sudden peak current in Fig. 23. A zoomed plot of the current consumption is shown in Fig. 24, where the current consumptions for the deep sleep mode, the awake mode, and the motor control mode are clearly distinguished. The deep sleep mode consumes approximately 25 mA and lasts for 8 s, after which the Arduino Uno is woken up by its internal clock and measures the temperature from the connected thermometer. The awake mode takes less than 1 s and consumes 37 mA on average. When the temperature requirement is met and the motor control is activated, an intravenously current increase to 270 mA is observed and lasts for about 2 s, which corresponds to 6 Joule of energy in total. The overall energy consumption of the controlling unit is shown in Table 4. The deep sleep mode, the awake mode, and the motor control mode consumes 0.30, 0.44, and 3.24 W of power, respectively. It is worth to mention that the 12 V battery pack is connected directly to the Arduino Uno, which enlarges the power consumption. Less power is expected if a high-efficiency step-down voltage converter is added between the battery and the Arduino Uno.

In the scope of this research, the flexibility and the extensibility outweigh the improvement of the energy consumption and therefore the Arduino Uno is chosen for its outstanding flexibility of general-purpose use. An application-specific microcontroller is preferred for future projects to increase specific performance or reduce power consumption. For example, the ESP 32 can be used as a centralized control-unit for ultra-low power consumption need, or wireless data communication requirement through the integrated Bluetooth Low Energy (BLE) or Wi-Fi module. One advantage of this flexible setup is that multiple windows can be controlled simultaneously by one microcontroller. As the DS18B20 digital temperature sensor supports 'one wire' communication protocol, several sensors can be attached to a single data pin on the microcontroller with separate readings. The motor adjustment can be individualized via several L298N H-bridge components. Therefore, the power consumption and the hardware cost will be averaged over multiple window blinds, which improves the energy efficiency and robustness of the smart window management system.
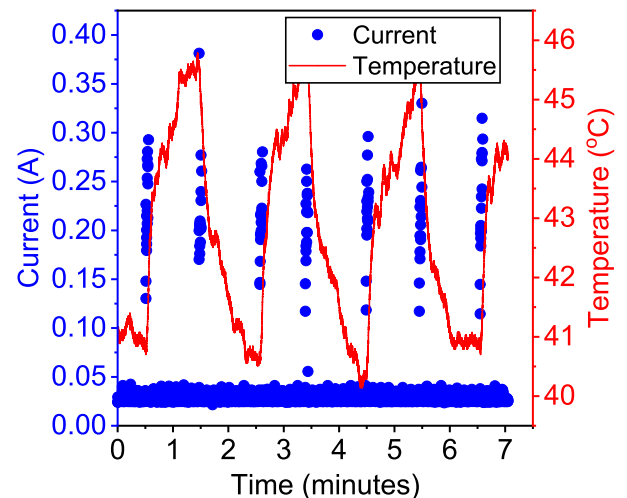

Fig. 23. The temperature measurement and the system energy consumption of the smart window blinds.
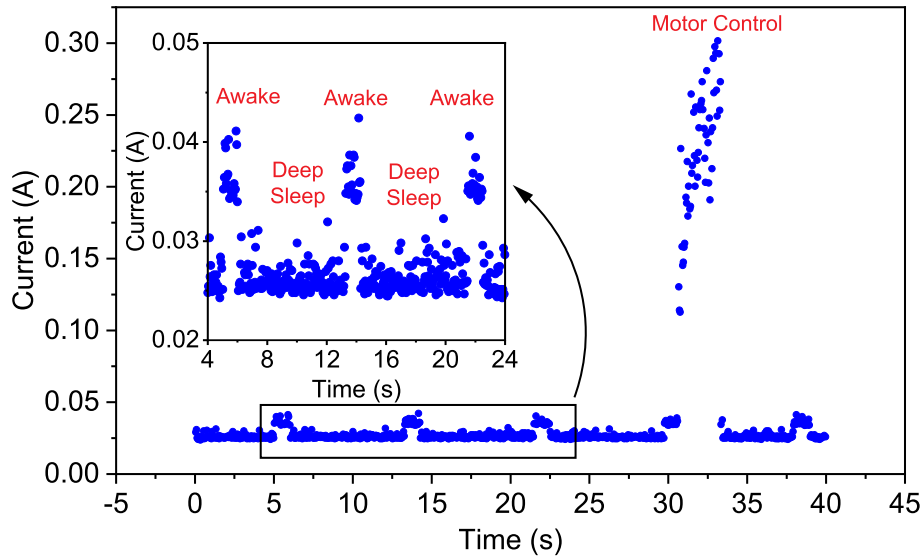
Fig. 24. The detailed energy consumption for deep sleep, awake and the motor control mode.

Table 4
Energy consumption of the smart window blinds controlling unit.

	Deep sleep	Awake	Motor control
Voltage (V)	12	12	12
Current (mA)	25	37	270
Power (W)	0.30	0.44	3.24

4. Energy availability and equilibrium design

The test performance of the prototype serves as a valuable reference for the self-powered design and analysis in this section. The full potential of the solar irradiation on window blinds is carefully analyzed in Subsection 4.1, so as to quantify the energy harvesting power of the SPSWB. The energy equilibrium analysis is proposed in Subsection 4.2 based on the test data in the previous section and is followed by a case study in New York City in Subsection 4.2. It is discovered that the energy harvesting capability far outweighs the power needed for the operations, which proves the feasibility and the robustness of the system.

4.1. Solar irradiation on window blinds

For the energy harvesting design, the energy availability analysis is always the first step to determine how much power could be potentially harvested. The traditional solar designs refer to the solar map for the estimation of the solar electric potential. However, the data of the solar map is applicable for the panels mounted on the flat surface with no shading and obstacles. For the PV cells attached on the window blinds, a specific analysis is required to determine the I_{siwb}, the direct solar irradiation on window blinds. The I_{siwb} is originated from the direct solar irradiation from the sun. One estimation is to start directly from the irradiation from the sun, and combined with the sun zenith angle, which varies by time and date, to determine the available irradiation. However, this approach does not incorporate local weather conditions, which can possibly affect the available solar irradiation. Moreover, it needs to incorporate the data at different time of a single day, which is too complicated to model precisely. A more practical approach is to estimate based on the local solar energy stations, which has already considered the local weather conditions and

the sunlight angle at different time by providing an averaged data over a month.

Empirically, the Average Tilt at Latitude (ATaL) angle will often produce the highest energy output [34], which is defined as the total amount of solar radiation received per unit area by a surface that is tilted toward the equator at an angle equal to the current latitude. Therefore, it is used to calculate the direct solar irradiation from the sun, to incorporate all local influences.

Theoretically, the optimal angle for the solar energy harvesting is the plane perpendicular to the solar irradiation, as indicated by the dash line in Fig. 25. The earth's axis results in an angle between the earth–sun line and the earth's equatorial plane, and is called the solar declination ξ, which ranges from –23.45° to 23.45° from winter to summer and is represented as [35]:

$$\xi = 23.45 \sin\left[\frac{2\pi}{365}(284 + N)\right] \tag{1}$$

where N is the date of a year starting from January 1st. The geographical location is represented by the local latitude ϕ, ranging from –90° to 90° from the south pole to the north.

With the help of the solar declination and the local latitude, the maximum solar irradiation I_0 that can be received by the dash line in Fig. 25 is determined via the ATaL position measurement I_{ATaL} as

$$I_0 = \frac{I_{ATaL}}{\cos \xi} \tag{2}$$

Considering that the buildings are perpendicular to the ground, the placement of the window blinds is vertical, which is represented by the green line in Fig. 25. The maximum rotational angle of the window blinds θ, as indicated in Fig. 21 should also be considered. Therefore, the solar irradiation perpendicular to the window blinds can be calculated as

$$I_{siwb} = I_0 \cos \alpha = I_{ATaL} \frac{\cos\left(\phi + \xi - \frac{\theta}{2}\right)}{\cos \xi} \tag{3}$$

It is worth to mention that the I_{siwb} defined in Eq. (3) can be maximized by a proper manipulation of the rotational angle $\tilde{\theta}$ $\left(-\theta/2 \leq \tilde{\theta} \leq \theta/2\right)$. Two insights can be derived from Eq. (3) to aid the control algorithm for the smart window blinds:

1) Given the maximum rotational range θ of a window blinds, the region where a perpendicular solar irradiation could be
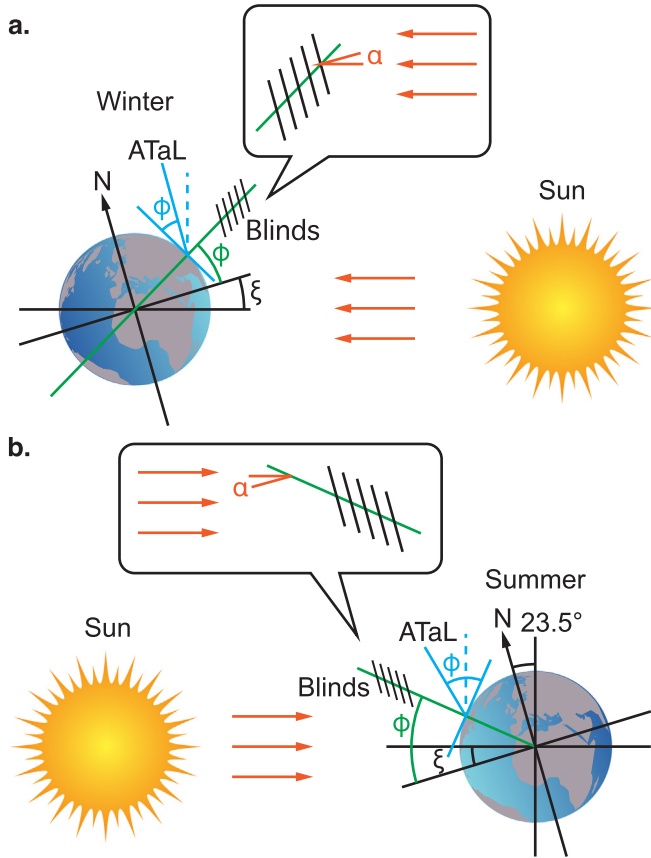
Fig. 25. Sunlight and window blinds angle in a. winter and b. summer.

achieved in any date of a year is determined by setting the $\alpha = 0$, which gives the latitude

$$\phi = \frac{\theta}{2} - \xi \tag{4}$$

Therefore, the regions with latitude $-48.55° \leqslant \phi \leqslant 48.55°$ can always get the direct solar irradiation in any dates of a year with a proper control of the blind slats' direction;

2) Given the location latitude ϕ, the range of dates with direct solar irradiation could be determined by a proper manipulation of the rotational angle $\tilde{\theta}$ and the solar declination ξ. By combining Eq. (1) and (3), the proper angle of the rotation $\tilde{\theta}$ could be determined with respect to the date N to guarantee the optimal power harvesting of the solar energy:

$$\tilde{\theta} = 2\phi + 46.9° \sin\left[\frac{2\pi}{365}(284 + N)\right], \tilde{\theta} \in \left[-\frac{\theta}{2}, \frac{\theta}{2}\right] \tag{5}$$

Therefore, the optimal state of solar energy harvesting on window blinds is achieved by a proper controlling algorithm with the pre-knowledge of location latitude and the tracking of the date.

Notice that the measurements from the solar station are based on the south-facing solar panels in an open space. Further studies are needed to quantify the reduction factors of the solar irradiation for scenarios like the non-south facing of the window, the atmosphere scattering, and the light reflection from surrounding architectures.

4.2. Energy equilibrium analysis

The self-powered function is an important feature for the proposed sun-powered smart window blinds, after which the abundant energy can be used as the power output for small appliances or more complicated monitoring and smart controls. Therefore, the energy equilibrium analysis of the solar energy harvesting and the system power consumption is an essential step. The energy level in the battery is traced throughout a prescribed period T, which is typically a year, to aid the engineering design and to predict the system performance. The amount of energy charged into the battery E_{bat} is decomposed into the harvested power P_{har} and the consumed power P_{con} as described below

$$E_{bat} = (P_{har} - P_{con}) \times T \tag{6}$$

where P_{har} and P_{con} are described in detail below. A case study based on New York City measurements will be discussed as an example of the energy equilibrium design and engineering. The power harvested and stored into the battery comes from the photovoltaic cells on the window blinds, and is written as

$$P_{har} = I_{siwb} \times A_{PV} \times \eta_{PV} \times \eta_{BM} \tag{7}$$

where I_{siwb} is the solar irradiation on window blinds as determined in Section 4.1, A_{PV} is the area of the photovoltaic cells, η_{PV} and η_{BM} represent the energy efficiency of the photovoltaic cells and the battery management system, correspondingly. The area of the photovoltaic cells A_{PV} depends on the applications and the current window size of $A_{PV} = 0.9\,\text{m} \times 1.5\,\text{m} = 1.35\,\text{m}^2$ is used for estimation. The efficiencies of $\eta_{PV} = 2\%$ and $\eta_{BM} = 55\%$ is measured based on the tests conducted in Chapter 2.

The energy consumption of the system is majorly comprised of the actuator, the sensor and the microcontroller, in which the consumed power P_{con} is defined as:

$$P_{con} = P_{act} + P_{sen} + P_{ctl} \tag{8}$$

In the scope of this research, the power consumption from the sensors P_{sen} is minimal compared with the other two power consumptions and could be neglected. The motor is responsible for all the actuations such as the rotational and translational motion and corresponding power consumption could be decomposed correspondingly. The consumption of the microcontroller is segmented by the status of the microcontroller into the awake mode and the deep sleep mode. Therefore, the consumed power P_{con} is written as:

$$P_{con} = P_{MOT} + P_{CTL} = P_{mo}\left(\frac{t_{rot}}{T_{rot}} + \frac{t_{trans}}{T_{trans}}\right) + \frac{P_{aw}t_{aw} + P_{ds}t_{ds}}{t_{aw} + t_{ds}} \tag{9}$$

where P_{mo} is the power consumption of the motor for both rotational and translational motions, which consumes equal amount of energy according to the test; t_{rot} and t_{trans} are the time taken for a rotational or translational motion correspondingly, within a prescribed period T_{rot} and T_{trans}; P_{aw}, t_{aw}, P_{ds}, and t_{ds} are the power consumption and time for the awake and deep sleep mode correspondingly.

The motion of the blinds is automated by the microcontroller and is related to the prescribed temperature thresholds, the surrounding environments, and human interactions. The activation of a rotation will take approximately 2 s with the averaged power consumption of 3.24 W, from which $t_{rot} = 2$ s and P_{mo} = 3.24 W are obtained. The period T_{rot} is the averaged time needed for a single activation of the rotation and is dependent on the prescribed temperature thresholds and the surrounding environment. One design methodology is to prescribe the temperature thresholds, so that the T_{rot} can be determined depending on the surrounding environment. This methodology would require rigorous testing in different

environments. Another methodology is to prescribe the T_{rot} so as to prescribe how many rotations will occur within a certain period of time. With this approach, the temperature thresholds can be calculated afterward and updated continuously based on the surroundings. In the second approach, machine learning algorithms can be implemented to predict the temperature threshold based on either the temperature prediction from the Internet, or the local environmental measurements from the attached sensors. In the scope of this research, the T_{rot} is prescribed as 1 min from the test conducted in Fig. 23, suggesting that the rotational control of the blinds is activated every 1 min on average. The T_{rot} in the real application will be much shorter because of the weaker solar irradiation and better air ventilation. The translational motion of the blinds, including the lifting and lowering of the blinds, is highly dependent on human interference and is difficult to predict. Therefore, the translational motion by human interaction is neglected in the scope of this study. Unlike the motor, the power consumption from the microcontroller, which is divided into the deep sleep mode and the awake mode, is more stable and less influenced by the surroundings. The ratio between the deep sleep time and the awake time $\gamma = t_{ds}/t_{aw}$ can be defined to control the power consumption from the microcontroller. Therefore, the Eq. (9) can be further simplified as:

$$P_{con} = P_{mo}\frac{t_{rot}}{T_{rot}} + \left[P_{ds} + (P_{aw} - P_{ds})\frac{1}{1+\gamma}\right] \quad (10)$$

in which the period of the rotational motion T_{rot} and the ratio between the deep sleep time and the awake time γ are two variables to control the overall power consumption.

4.3. SPSWB case study in New York City

New York City is chosen as a demonstration of the energy equilibrium analysis. The average energy received per day in each month is obtained from the local solar energy stations [34] by considering the ATaL angle between the sunlight and solar panels. The latitude ϕ of New York City is obtained, and the average solar declination angle ξ is calculated with the help of Eq. (1). The projected energy onto the window blinds, which is listed in Table 5, is therefore calculated with through Eq. (2) and (3). The solar irradiation intensity $I_i(i = ATaL, 0, siwb)$ can be directly calculated from the $E_i(i = ATaL, 0, siwb)$ by dividing 24 h/day as the average over a day. The average energy received by the ATaL angle E_{ATaL}, the optimal angle E_0, and the window blinds E_{siwb} are plotted in Fig. 26 for a straightforward distribution over months. It is illustrated that the solar irradiation reaches its peak value during summer, which can be best described by the fact that the available energy in the

summer is above 2.5 times as high as the lowest available energy during winter. It is also interesting to point out that in the summertime in the northern hemisphere, the sunlight is almost in parallel with the vertical building skins, which could potentially waste the abundant solar energy if the PV is attached directly to the building skin. However, a placement angle θ is introduced by the design of the window blinds, as described in Fig. 21, and this angle compensates the harm from the vertical building skin and brings the PV cells closer to the direct solar irradiation. When the α in Table 5 is negative, the perpendicular solar irradiation onto the window blinds can be achieved by adjusting the rotational angle of the motor, and therefore achieving the optimal solar energy harvesting from the photovoltaic cells.

The harvested power into the battery P_{har} can be calculated from the E_{siwb} in Table 5, with the help of Eq. (7). The consumed power from the battery P_{con} is determined from the Eq. (10), with the prescribed $\gamma = 7$ and $T_{rot} = 1$ min obtained from the tests. The harvested, consumed power is listed in Table 6, together with the projected energy that can be saved in a month. It is concluded that the harvested power is much larger than the power needed for the motor and microcontroller, and the energy equilibrium can be easily satisfied with any sized battery. The power efficiency of the system, defined as the remaining power divided by the total harvested power, is between 70% and 90%, indicating that the harvested power is 3 to 9 times larger than the needed power from the motor and the controller. In terms of a precise estimation and evaluation, reduction factors are needed for the blinds facing other directions, the light diffusion and reflection in high rise buildings. However, the abundant energy in Table 6 provides a promising future for the application of the SPSWB system.

The efficiency could be improved by the larger rotational period T_{rot}, via the optimization of the temperature control, or a better microcontroller with less deep sleep consumption, such as the ESP 32 introduced in Chapter 5. Since the power consumption of the deep sleep mode for the Arduino Uno R3 is not obviously different to the awake mode, the increase of the sleep-awake ratio γ will not improve the energy consumption significantly. The monthly saved energy is also calculated to quantify the amount of energy charged into the battery, serving as an indicator of the energy budget for the translational motion of the window blinds and for other connected devices in the future. The abundant energy projection validates the feasibility of the design and indicates the great application potentials, from creating a platform for a wide range of sensors to serving as an energy hub of various smart home devices in the future. Notice that all the electronic components of the proposed SPSWB system are commerically available and cost less than $50 in total. The major investment comes from the thin-film

Table 5
Solar irradiation and angles in New York City.

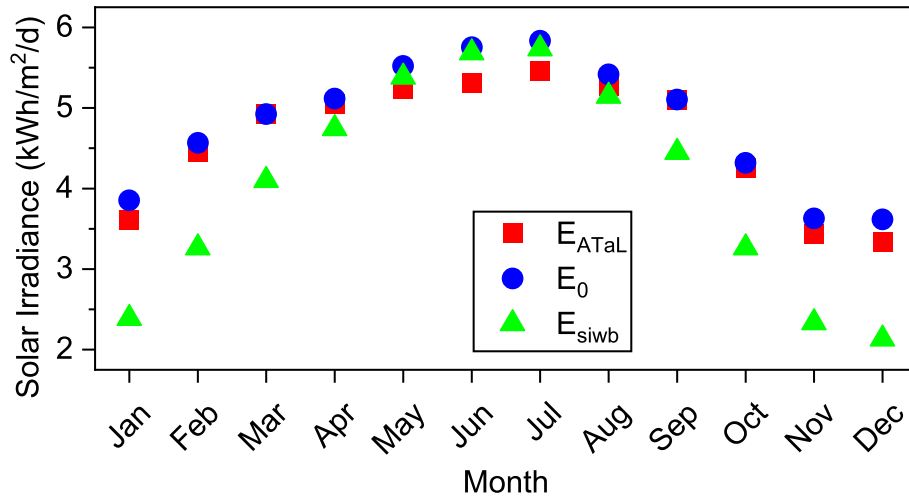| Month	Jan	Feb	Mar	Apr	May	Jun
E_{ATaL} (kWh/m^2)	3.61	4.45	4.92	5.05	5.24	5.31
$\zeta(°)$	−20.40	−13.09	−2.34	9.30	18.40	22.61
$\phi_{NY}(°)$	40.72	40.72	40.72	40.72	40.72	40.72
E_0(kWh/m^2/d)	3.85	4.57	4.92	5.12	5.52	5.75
$\alpha(°)$	−51.68	−44.38	−33.62	−21.98	−12.88	−8.67
E_{siwb}(kWh/m^2/d)	2.39	3.27	4.10	4.75	5.38	5.69
Month	Jul	Aug	Sep	Oct	Nov	Dec
E_{ATaL} (kWh/m^2/d)	5.46	5.28	5.10	4.26	3.44	3.34
$\zeta(°)$	20.65	13.01	1.95	−9.64	−18.67	−22.60
$\phi_{NY}(°)$	40.72	40.72	40.72	40.72	40.72	40.72
E_0(kWh/m^2/d)	5.83	5.42	5.10	4.32	3.63	3.62
$\alpha(°)$	−10.64	−18.27	−29.33	−40.92	−49.95	−53.88
E_{siwb}(kWh/m^2/d)	5.73	5.15	4.45	3.27	2.34	2.13

Fig. 26. Average Tilt at Latitude, direct, and window blinds solar irradiation in New York.

Table 6
Harvested, consumed and saved energy of the smart window blind.

Month	Jan	Feb	Mar	Apr	May	Jun
E_{siwb} (kWh/m^2/d)	2.39	3.27	4.10	4.75	5.38	5.69
η_{PV}	0.02	0.02	0.02	0.02	0.02	0.02
η_{BM}	0.55	0.55	0.55	0.55	0.55	0.55
Area (m^2)	1.50	1.50	1.50	1.50	1.50	1.50
P_{har}(W)	1.64	2.25	2.82	3.26	3.70	3.91
P_{MOT}(W)	0.11	0.11	0.11	0.11	0.11	0.11
P_{CTL}(W)	0.32	0.32	0.32	0.32	0.32	0.32
P_{con}(W)	0.43	0.43	0.43	0.43	0.43	0.43
P_{remain}(W)	1.22	1.82	2.39	2.84	3.28	3.48
Efficiency	0.74	0.81	0.85	0.87	0.89	0.89
Monthly saved energy(kWh/M)	0.88	1.31	1.72	2.04	2.36	2.51
Month	Jul	Aug	Sep	Oct	Nov	Dec
E_{siwb} (kWh/m^2/d)	5.73	5.15	4.45	3.27	2.34	2.13
η_{PV}	0.02	0.02	0.02	0.02	0.02	0.02
η_{BM}	0.55	0.55	0.55	0.55	0.55	0.55
Area (m^2)	1.50	1.50	1.50	1.50	1.50	1.50
P_{har}(W)	3.94	3.54	3.06	2.24	1.61	1.47
P_{MOT}(W)	0.11	0.11	0.11	0.11	0.11	0.11
P_{CTL}(W)	0.32	0.32	0.32	0.32	0.32	0.32
P_{con}(W)	0.43	0.43	0.43	0.43	0.43	0.43
P_{remain}(W)	3.52	3.11	2.63	1.82	1.18	1.04
Efficiency	0.89	0.88	0.86	0.81	0.74	0.71
Monthly saved energy(kWh/M)	2.53	2.24	1.90	1.31	0.85	0.75

photovoltaic cells, due to its relatively high price and low energy conversion rate. The third generation of thin-film photovoltaic cells have been under active development in the recent decade, and some of the thin-film cells have achieved more than 21% of energy conversion rate in the laboratory [36]. The team is preparing to use perovskite cells in future commercialization, which will increase the energy efficiency and reduce the total cost of the system.

5. Conclusions

A novel sun-powered smart window blinds system is designed, fabricated and tested, with the flexible photovoltaic cells attached on one side and PVdF-HFP passive cooling coating attached on the other side. The smart controlling system is also integrated for the environmental sensing and active response, to ensure the optimal performance in different conditions. The system harvests green energy from solar irradiation, self-powers the connected sensors, controllers, and actuators, and informs the next generation of smart BIPV system.

Comprehensive tests are conducted to quantify the performance of the flexible PV cells, and its linear relation to the temperature and the solar irradiation. The open-circuit voltage, short-circuit current, and the optimal power output are measured via a commercial solar tracer, such that the optimal power output and the corresponding external resistance can always be determined given the applied solar irradiation and the temperature. The energy efficiency of the flexible PV cell is around 2% according to the test measurements, which is due to its thin thickness, physical flexibility, and the overlap of the window blinds. The cooling performance of the PVdF-HFP passive cooling coating is also quantified via the stable temperature measurement under different solar irradiation, where a temperature reduction ranging from 4% to 9% is observed thanks to the coating. A better performance can be anticipated in the real application thanks to the better air ventilation. Due to the intermittency of the solar energy, the voltage regulation and battery management systems are designed and tested with a 12 V 18650 battery pack. Two tests are conducted under different solar irradiation intensities and a stable efficiency of 55% is

achieved in the energy delivery process from the PV into the battery. The controlling system is built based on the Arduino Uno R3 microcontroller and connected to a thermometer for the temperature measurement. Automated control of the window blinds is achieved depending on the prescribed temperature thresholds and the current temperature measurement. The deep sleep mode is activated, and the corresponding energy consumptions are recorded in each phase. The methodology to predict the solar irradiation potential onto the window blinds is proposed and discussed, which utilizes the measurements from local solar energy stations to incorporate the influence of local weather conditions and solar zenith angles within a day. The methodology determines the region with the direct solar irradiation over the year and offers of the optimal angle to receive the direct sunlight. The energy equilibrium analysis is proposed based on the testing data. The energy harvesting capability of the smart window blinds far outweighs the power needed for the controller and the motor, and the abundant energy validates the feasibility and robustness of the system and proves its broad utilization for an extensive range of sensors and applications.

Given the success of the prototype testing and energy equilibrium analysis, further improvements could be achieved on the followings topics: the energy conversion efficiency could be improved via a proper engineering of the buck-boost converter; the optimal temperature thresholds could be tailored for different conditions via the thermal analysis of the window blinds to the internal and external environment; further studies are needed to quantify the reduction factors of the non-south facing conditions and other environmental compromises. Notice that the PV-integration changes the outlook of the window blinds, which may face potential resistance from the building architects and owners. Although it could be alleviated by colored or transparent PV, its influence cannot be fully eliminated, and the energy harvesting performance will also be compromised. In order to protect the vulnerable coating and the controlling system, the proposed SPSWB system sits insides the window structure between the glazing, which limits its application only to the thick window frames. Therefore, an independent SPSWB system shall be engineered to fit the various types of window frames. Overall, the SPSWB is proved to be a feasible and robust system, and the corresponding experimental results will inform the next generation of the smart BIPV systems.

CRediT authorship contribution statement

Qiliang Lin: Methodology, Data curation, Writing - original draft. **Yanchu Zhang:** Methodology, Writing - review & editing. **Arnaud Van Mieghem:** Investigation, Validation. **Yi-Chung Chen:** Methodology, Supervision. **Nanfang Yu:** Conceptualization, Project administration. **Yuan Yang:** Conceptualization, Project administration. **Huiming Yin:** Funding acquisition, Conceptualization, Project administration.

Declaration of Competing Interest

The authors declare that they have no known competing financial interests or personal relationships that could have appeared to influence the work reported in this paper.

Acknowledgement

Appendix A. Supplementary data

Supplementary data to this article can be found online at https://doi.org/10.1016/j.enbuild.2020.110173.

References

[1] US Department of Energy, Quadrennial Technology Review 2015-An Assessment of Energy Technologies and Research Opportunities, Chapter 5: Increasing Efficiency of Building Systems and Technologies, US Department of Energy, 2015.

[2] Energy Information Administration (EIA), Manufacturing Energy Consumption Survey 2010, Washington DC, 2013.

[3] Energy Information Administration (EIA), Annual Energy Review 2014-With Projections to 2040, Department of Energy, Washington, DC: U.S, 2014. http://www.eia.gov/outlooks/archive/aeo14/pdf/0383(2014).

[4] M.A. Berawi, P. Miraj, M.S. Sayuti, A.R.B. Berawi, Improving building performance using smart building concept: Benefit cost ratio comparison, AIP Conf. Proc. 1903 (2017), https://doi.org/10.1063/1.5011508 030001.

[5] P.H. Shaikh, N.B.M. Nor, P. Nallagownden, I. Elamvazuthi, T. Ibrahim, A review on optimized control systems for building energy and comfort management of smart sustainable buildings, Renew. Sustain. Energy Rev. 34 (2014) 409–429, https://doi.org/10.1016/j.rser.2014.03.027.

[6] D.L. Marino, K. Amarasinghe, M. Manic, Building energy load forecasting using Deep Neural Networks, in: IECON 2016 - 42nd Annual Conference of the IEEE Industrial Electronics Society, 2016: pp. 7046–7051. https://doi.org/10.1109/IECON.2016.7793413.

[7] L. Wang, E.W.M. Lee, R.K.K. Yuen, Novel dynamic forecasting model for building cooling loads combining an artificial neural network and an ensemble approach, Appl. Energy 228 (2018) 1740–1753, https://doi.org/10.1016/j.apenergy.2018.07.085.

[8] M.Q. Raza, A. Khosravi, A review on artificial intelligence based load demand forecasting techniques for smart grid and buildings, Renew. Sustain. Energy Rev. 50 (2015) 1352–1372, https://doi.org/10.1016/j.rser.2015.04.065.

[9] Z. Chen, C. Jiang, L. Xie, Building occupancy estimation and detection: A review, Energy Build. 169 (2018) 260–270, https://doi.org/10.1016/j.enbuild.2018.03.084.

[10] F.K. Shaikh, S. Zeadally, Energy harvesting in wireless sensor networks: A comprehensive review, Renew. Sustain. Energy Rev. 55 (2016) 1041–1054, https://doi.org/10.1016/j.rser.2015.11.010.

[11] S. Sharma, K.K. Jain, A. Sharma, Solar Cells. In Research and Applications—A Review, Materials Sciences and Applications. 6 (2015) 1145–1155, https://doi.org/10.4236/msa.2015.612113.

[12] M.A. Green, Thin-film solar cells: review of materials, technologies and commercial status, J Mater Sci: Mater Electron. 18 (2007) 15–19, https://doi.org/10.1007/s10854-007-9177-9.

[13] J. Yan, B.R. Saunders, Third-generation solar cells: a review and comparison of polymer:fullerene, hybrid polymer and perovskite solar cells, RSC Adv. 4 (2014) 43286–43314, https://doi.org/10.1039/C4RA07064J.

[14] C. Peng, Y. Huang, Z. Wu, Building-integrated photovoltaics (BIPV) in architectural design in China, Energy Build. 43 (2011) 3592–3598, https://doi.org/10.1016/j.enbuild.2011.09.032.

[15] A.K. Shukla, K. Sudhakar, P. Baredar, A comprehensive review on design of building integrated photovoltaic system, Energy Build. 128 (2016) 99–110, https://doi.org/10.1016/j.enbuild.2016.06.077.

[16] F. Chen, H. Yin, Fabrication and laboratory-based performance testing of a building-integrated photovoltaic-thermal roofing panel, Appl. Energy 177 (2016) 271–284, https://doi.org/10.1016/j.apenergy.2016.05.112.

[17] H.M. Yin, D.J. Yang, G. Kelly, J. Garant, Design and performance of a novel building integrated PV/thermal system for energy efficiency of buildings, Sol. Energy 87 (2013) 184–195, https://doi.org/10.1016/j.solener.2012.10.022.

[18] M.S. Buker, B. Mempouo, S.B. Riffat, Experimental investigation of a building integrated photovoltaic/thermal roof collector combined with a liquid desiccant enhanced indirect evaporative cooling system, Energy Convers. Manage. 101 (2015) 239–254, https://doi.org/10.1016/j.enconman.2015.05.026.

[19] V. Delisle, M. Kummert, A novel approach to compare building-integrated photovoltaics/thermal air collectors to side-by-side PV modules and solar thermal collectors, Sol. Energy 100 (2014) 50–65, https://doi.org/10.1016/j.solener.2013.09.040.

[20] T.N. Anderson, M. Duke, G.L. Morrison, J.K. Carson, Performance of a building integrated photovoltaic/thermal (BIPVT) solar collector, Sol. Energy 83 (2009) 445–455, https://doi.org/10.1016/j.solener.2008.08.013.

[21] Q. Lin, F. Chen, H. Yin, Experimental and theoretical investigation of the thermo-mechanical deformation of a functionally graded panel, Eng. Struct. 138 (2017) 17–26, https://doi.org/10.1016/j.engstruct.2017.01.062.

[22] Lin Qiliang, Zhang Liangliang, Chen Fangliang, Yin Huiming, Micromechanics-Based Elastoplastic Modeling of Functionally Graded Materials with Pairwise Particle Interactions, J. Eng. Mech. 145 (2019) 04019033, https://doi.org/10.1061/(ASCE)EM.1943-7889.0001603.

[23] P.K. Ng, N. Mithraratne, H.W. Kua, Energy analysis of semi-transparent BIPV in Singapore buildings, Energy Build. 66 (2013) 274–281, https://doi.org/10.1016/j.enbuild.2013.07.029.

[24] L. Lu, K.M. Law, Overall energy performance of semi-transparent single-glazed photovoltaic (PV) window for a typical office in Hong Kong, Renewable Energy 49 (2013) 250–254, https://doi.org/10.1016/j.renene.2012.01.021.

[25] P.K. Ng, N. Mithraratne, Lifetime performance of semi-transparent building-integrated photovoltaic (BIPV) glazing systems in the tropics, Renew. Sustain. Energy Rev. 31 (2014) 736–745, https://doi.org/10.1016/j.rser.2013.12.044.

[26] J. Peng, D.C. Curcija, A. Thanachareonkit, E.S. Lee, H. Goudey, S.E. Selkowitz, Study on the overall energy performance of a novel c-Si based semitransparent solar photovoltaic window, Appl. Energy 242 (2019) 854–872, https://doi.org/10.1016/j.apenergy.2019.03.107.

[27] B. Fina, H. Auer, W. Friedl, Profitability of active retrofitting of multi-apartment buildings: Building-attached/integrated photovoltaics with special consideration of different heating systems, Energy Build. 190 (2019) 86–102, https://doi.org/10.1016/j.enbuild.2019.02.034.

[28] M.S. Karimi, F. Fazelpour, M.A. Rosen, M. Shams, Techno-economic feasibility of building attached photovoltaic systems for the various climatic conditions of Iran, Environmental Progress & Sustainable Energy. 0 (n.d.) e13239. https://doi.org/10.1002/ep.13239.

[29] X. Wu, Y. Liu, J. Xu, W. Lei, X. Si, W. Du, C. Zhao, Y. Zhong, L. Peng, J. Lin, Monitoring the performance of the building attached photovoltaic (BAPV) system in Shanghai, Energy Build. 88 (2015) 174–182, https://doi.org/10.1016/j.enbuild.2014.11.073.

[30] H. Saini, R.C.G.M. Loonen, J.L.M. Hensen, Simulation-based performance prediction of an energy-harvesting facade system with selective daylight transmission, in: VIII International Congress on Architectural Envelopes, 2018: pp. 213–219. https://research.tue.nl/en/publications/simulation-based-performance-prediction-of-an-energy-harvesting-f-2 (accessed October 14, 2019).

[31] C. Koo, T. Hong, K. Jeong, C. Ban, J. Oh, Development of the smart photovoltaic system blind and its impact on net-zero energy solar buildings using technical-economic-political analyses, ENERGY. 124 (2017) 382–396, https://doi.org/10.1016/j.energy.2017.02.088.

[32] PowerFilm Solar OEM Components - Frequently Asked Questions | FlexSolarCells, (n.d.). http://www.flexsolarcells.co.uk/index_files/OEM_Components/PowerFilm-Solar-OEM-Components-FAQs.php (accessed December 16, 2019).

[33] J. Mandal, Y. Fu, A.C. Overvig, M. Jia, K. Sun, N.N. Shi, H. Zhou, X. Xiao, N. Yu, Y. Yang, Hierarchically porous polymer coatings for highly efficient passive daytime radiative cooling, Science 362 (2018) 315–319, https://doi.org/10.1126/science.aat9513.

[34] Solar Energy and Solar Power in New York, NY, Solar Energy Local. (n.d.). https://www.solarenergylocal.com/states/new-york/new-york/ (accessed December 28, 2019).

[35] Solar Altitude Angle - an overview | ScienceDirect Topics, (n.d.). https://www.sciencedirect.com/topics/engineering/solar-altitude-angle (accessed December 28, 2019).

[36] K. Wang, D. Yang, . Wu, M. Sanghadasa, S. Priya, Recent progress in fundamental understanding of halide perovskite semiconductors, Progress in Materials Science 106 (2019), https://doi.org/10.1016/j.pmatsci.2019.100580. In this issue.

[37] Q. Lin, Y-C. Chen, F. Chen, T. DeGanyar, H. Yin, Design and experiment of a thermoelectric-powered wireless sensor network platform for smart building envelope, Applied Energy (2020) Submitted for publication.